

Simultaneous reconstruction of internal tissue region boundaries and coefficients in optical diffusion tomography

V Kolehmainen[†], S R Arridge[‡], M Vauhkonen[†] and J P Kaipio[†]

[†] Department of Applied Physics, University of Kuopio, PO Box 1627, 70211 Kuopio, Finland

[‡] Department of Computer Science, University College London, Gower Street, London WC1E 6BT, UK

E-mail: kaipio@venda.uku.fi

Received 24 January 2000, in final form 6 July 2000

Abstract. In this paper we propose a new numerical method to the inverse problem in optical diffusion tomography. We consider the reconstruction of the diffusion and absorption coefficients (κ , μ_a) within a domain Ω which is known to consist of a set of disjoint regions of distinct tissue types. The assumption is that the regions of different tissues are bounded by smooth boundary curves and have constant absorption and diffusion coefficients. The goal in the proposed method is to reconstruct simultaneously the boundaries of the tissue regions together with the absorption and diffusion coefficients within these regions. The solution of the problem is based on the finite element method and subdivision of the elements. The performance of the proposed method is evaluated by simulations in which the optical parameters (κ , μ_a) are relevant in medical applications of optical tomography. It is shown that the proposed method is able to recover both the boundaries and the coefficients with good accuracy.

1. Introduction

By optical (diffusion) tomography we mean the use of visible or near-infrared light in the wavelength range ~ 700 – 1000 nm, to probe highly scattering media in order to derive images of the diffusion and absorption coefficients (κ , μ_a) within an object Ω . Of the potential applications, the most attention has been paid to medical imaging, such as detection of breast cancer (Fantini *et al* 1996, Moesta *et al* 1998, Jess *et al* 1996) and monitoring infant brain tissue oxygenation level (Arridge and Schweiger 1999, van Houten *et al* 1996, Wyatt *et al* 1990).

In the measurement setup S optic fibres are placed on the source positions $\varepsilon_j \subset \partial\Omega$ on the boundary of the object Ω , and M optic fibres are placed in the measurement positions $\zeta_i \subset \partial\Omega$. In optical tomography the data can be acquired by using frequency-domain, intensity or time-resolved measurement systems. In frequency-domain systems light from a radio-frequency modulated source is guided via the optic fibres usually to one source location ε_j at the time, and the phaseshift and modulation amplitude of the transmitted light is measured at all measurement sites ζ_i using the optic fibres and light-sensitive detectors (Jiang *et al* 1995a). This process is then repeated for all source locations ε_j . Correspondingly, in the time-resolved systems an ultrashort input pulse (~ 10 ps) is triggered, usually to one source location ε_j at the time, and the impulse response function $\Gamma_{i,j}(t)$, which is often also referred to as the temporal point spread function (TPSF), of the object is measured on the detector locations ζ_i (Hebden *et al* 1997). The goal in optical tomography is to reconstruct images of the coefficients (κ , μ_a)

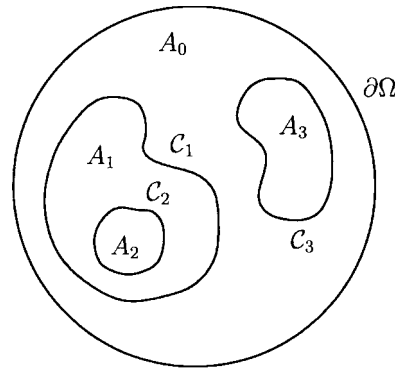


Figure 1. An example of a piecewise constant object domain $\Omega = \bigcup_k A_k$ with constant coefficients (κ_k, μ_{a_k}) , $k = 0, 1, 2, 3$. The outer boundaries of regions A_1 , A_2 and A_3 are denoted by C_1 , C_2 and C_3 , respectively. The background region A_0 has $\partial\Omega$ as the outer boundary.

within Ω based on the measurements made on the boundary $\partial\Omega$. In the frequency-domain systems the image reconstruction can be carried out by using the measured phaseshift and modulation amplitude as data, or alternatively, by using the real and imaginary parts of the reconstructed complex measurements $\Gamma_{i,j}(\omega)$ as the data (Jiang *et al* 1995a). Respectively, in the time-resolved systems the image reconstruction can be carried out by using the whole spatio-temporal measurement set (Gryazin *et al* 1999, Hielscher *et al* 1999), or alternatively by using some temporal integral transforms of the measured signals $\Gamma_{i,j}(t)$ as the data (Schweiger and Arridge 1997, 1999a, Arridge and Schweiger 1995). The reconstruction of κ and μ_a in optical tomography is a nonlinear inverse problem.

In this paper we consider the reconstruction of κ and μ_a in the case of an object domain $\Omega \in \mathbb{R}^2$ which is known to consist of $L + 1$ disjoint tissue regions A_k

$$\Omega = \bigcup_{k=0}^L A_k. \quad (1)$$

The regions A_k are assumed to be bounded by smooth closed boundary curves $\{C_\ell, \ell = 1, \dots, L\}$ and have constant values of the diffusion and absorption coefficients $\{\kappa_k, \mu_{a_k}, k = 0, 1, \dots, L\}$ (see figure 1). The outer boundary of the background region A_0 is $\partial\Omega$. Assume that some information on the ‘anatomy’, that is, on the shapes and locations of the boundaries $\{C_\ell, \ell = 1, \dots, L\}$ is missing.

We have previously proposed a methodology for the recovery of the shapes and locations of the region boundaries $\{C_\ell\}$ in the case of general elliptic partial differential equations (PDE) (Kolehmainen *et al* 1999). The proposed method was restricted to the cases in which $\partial\Omega$ and the values $\{\kappa_k, \mu_{a_k}\}$ of the piecewise constant coefficients (κ, μ_a) of the PDE were known *a priori*. The proposed boundary recovery methodology was applied to simulated optical tomography data (d.c. intensity). However, in biomedical applications of optical tomography the values $\{\kappa_k, \mu_{a_k}\}$ are seldom known *a priori*.

Based on the work of Kolehmainen *et al* (1999), we present an extension of the previously proposed method for optical tomography. The goal is to reconstruct both the shapes and locations of the region boundaries $\{C_\ell\}$ and the values of the coefficients $\{\kappa_k, \mu_{a_k}\}$ within different tissue regions $\{A_k\}$ based on the data on $\partial\Omega$. We again assume that $\partial\Omega$ is known *a priori*. In the proposed method the shapes and locations of the boundaries $\{C_\ell\}$ are approximated with a finite set γ of shape coefficients. The FEM discretization of the forward model, which is the diffusion approximation to the radiative transfer equation (RTE), is

formulated as a mapping from the shape coefficients γ and the values $\{\kappa_k, \mu_{ak}\}$ to the data on $\partial\Omega$. The inverse problem is then to find the representation γ of the internal boundary configuration and the values $\{\kappa_k, \mu_{ak}\}$ based on measured data. This inverse problem is approached as an optimization problem which seeks to minimize the residual norm between the measured and predicted data. One attraction of the proposed approach is that the dimension of the search space can be made smaller than with local basis function parametrization, and this potentially leads to a less ill-posed inverse problem.

The rest of this paper is organized as follows. In section 2 we give brief reviews for the parametrization γ we use for the region boundaries $\{C_\ell\}$ and for the diffusion approximation to the RTE. In section 2 we also describe the FEM discretization of the diffusion approximation. The discretization we use is based on the method we originally proposed in (Kolehmainen *et al* 1999) for general elliptic PDEs with real-valued solutions. In section 3 the inverse problem is formulated and an iterative process for solving this problem is discussed. In section 3 we also discuss briefly the data type we use for the image reconstruction. In section 4 the performance of the method is evaluated with realistic synthetic data. In section 5 we give conclusions and address some suggestions for future work.

2. Forward model

2.1. Representation of the boundaries $\{C_\ell\}$

In this paper we assume that the domains $\{A_k\} \in \Omega$ are simply connected and disjoint (i.e. $C_i \cap C_j = \emptyset, i \neq j$) (see figure 1). We also assume that the outer boundary of the region A_0 , that is $\partial\Omega$ is known and has the property $\partial\Omega \cap C_\ell = \emptyset \forall \ell$. If the outer boundaries $\{C_\ell, \ell = 1, 2, \dots, L\}$ of the regions $\{A_\ell\}$ are sufficiently smooth, they can be approximated in the form

$$\{C_\ell(s)\} = \begin{pmatrix} x_\ell(s) \\ y_\ell(s) \end{pmatrix} = \sum_{n=1}^{N_\theta} \begin{pmatrix} \gamma_n^{x_\ell} \theta_n^x(s) \\ \gamma_n^{y_\ell} \theta_n^y(s) \end{pmatrix}, \quad \ell = 1, \dots, L \tag{2}$$

where θ_n are periodic and differentiable basis functions with period 1. In this paper we express both coordinates of the curve as Fourier series with respect to the curve parameter s , that is, we use basis functions of the form

$$\begin{aligned} \theta_1^\alpha &= 1 \\ \theta_n^\alpha &= \sin\left(2\pi \frac{n}{2}(s + \phi^s)\right), \quad n = 2, 4, 6, \dots \\ \theta_n^\alpha &= \cos\left(2\pi \left(\frac{n-1}{2}\right)(s + \phi^s)\right), \quad n = 3, 5, 7, \dots \end{aligned} \tag{3}$$

where ϕ^s is the phase of the curve parameter and α denotes either x or y . Furthermore, let γ denote the vector of the shape coefficients, that is

$$\gamma = (\gamma_1^{x_1}, \dots, \gamma_{N_\theta}^{x_1}, \gamma_1^{y_1}, \dots, \gamma_{N_\theta}^{y_1}, \dots, \gamma_1^{x_L}, \dots, \gamma_{N_\theta}^{x_L}, \gamma_1^{y_L}, \dots, \gamma_{N_\theta}^{y_L})^T. \tag{4}$$

For more details on the properties of the boundary representation (2) and (3), see Kolehmainen *et al* 1999.

2.2. Diffusion approximation to the RTE

Although light transport in scattering media is properly modelled with the radiative transfer equation (RTE), most of the current approaches to optical tomography use the diffusion approximation (DA) to the RTE as the forward model which is also the approach we use

in this paper. There are a variety of different boundary conditions that have been used with the diffusion approximation (Schweiger *et al* 1995). In this paper we use the Robin type boundary condition which arises naturally from the derivation of the DA from the RTE. For the index-matched problem, the RTE specifies that no photons travel in an inward direction at the boundary, except for source terms. Since the DA approximates the photon flux only up to its first angular moment, the diffusion boundary condition becomes that a weighted combination of the integral (zeroth moment) and the cosine weighted integral (first moment) of the photon flux over *inward* directions is zero (Ishimaru 1978, Schweiger *et al* 1995, Aronson 1995). With this condition, the diffusion approximation can be expressed in the frequency-domain as

$$\begin{aligned} -\nabla \cdot \kappa \nabla \Phi(\omega) + \mu_a \Phi(\omega) + \frac{i\omega}{c} \Phi(\omega) &= q_0, \quad \mathbf{r} \in \Omega \\ \Phi(\omega) + 2\kappa \vartheta \frac{\partial \Phi(\omega)}{\partial \nu} &= g_s, \quad \mathbf{r} \in \partial\Omega \end{aligned} \quad (5)$$

where Φ is the photon density, μ_a is the absorption coefficient (mm^{-1}), $\kappa = [3(\mu_a + \mu'_s)]^{-1}$ (mm) is the diffusion coefficient, μ'_s is the reduced scattering coefficient (mm^{-1}), c is the speed of light in the medium, q_0 is the distribution of internal light sources, g_s is the distribution of boundary sources, ν is the boundary normal direction and ϑ is a coefficient due to the mismatch of the refractive indices in Ω and the surrounding medium (Schweiger *et al* 1995).

For source terms, the incidence of a collimated beam in the RTE, would naturally lead to a specification of both a photon density (the zeroth-moment expansion of this source) and a photon current (from the first moment). The former is mathematically a Dirichlet condition, and the latter a Neumann condition, whereas their linear combination is a Robin condition. Results have shown that differences in these models are only significant within very small distances from the input position (Schweiger *et al* 1995). The most commonly used source condition in the diffusion model is the Dirichlet condition, usually called the collimated source model (CS) in which we set $g_s = 0$ and the light source is modelled as an isotropic point source located at depth $1/\mu'_s$ below the source site ε_j (i.e. $q_0 \neq 0$). However, in this paper we use the diffuse boundary source model (DS) in which we set $q_0 = 0$ and g_s is of the form

$$g_{s_j} = \begin{cases} -4\Gamma_s & \mathbf{r} \in \varepsilon_j \\ 0 & \mathbf{r} \in \partial\Omega \setminus \varepsilon_j. \end{cases} \quad (6)$$

that is, the source is modelled as an inward directed diffuse photon current on the source site $\varepsilon_j \subset \partial\Omega$. In the diffusion model the measured flux at the measurement site $\zeta_i \subset \partial\Omega$ for the j th source is obtained as

$$\Gamma_{i,j}(\omega) = -\kappa(\zeta_i) \nu \cdot \nabla \Phi_j(\omega). \quad (7)$$

The diffusion approximation has been validated to give reasonable accuracy in scattering-dominated media ($\mu'_s \gg \mu_a$). For further details on the diffusion approximation to the RTE, see Chandrasekhar (1950), Davison (1957), Weinberg and Wigner (1958), Case and Zweifel (1967), Duderstadt and Martin (1979), Dorn (1998), Arridge (1999), Ackroyd (1997) and Ishimaru (1978).

2.3. FEM discretization of the diffusion equation

In the FEM approach the domain Ω is divided to P disjoint elements $\bigcup_{p=1}^P \Omega_p$, joined at D vertex nodes N_i . The solution Φ is approximated with a piecewise polynomial $\Phi^h = \sum_{i=1}^D \phi_i \varphi_i \in \mathcal{U}^h$, where \mathcal{U}^h is a finite dimensional subspace of an associated Sobolev space (see Brenner and Scott 1994).

Using the Galerkin method, that is, using the basis functions as test functions, we obtain the matrix equation

$$(K(\kappa) + C(\mu_a) + R + i\omega M)\Phi = G + F. \quad (8)$$

The entries of the system matrices are given by

$$K_{ij} = \sum_{k=0}^L \int_{\text{supp}(\varphi_i \varphi_j) \cap A_k} \kappa_k \nabla \varphi_i \cdot \nabla \varphi_j \, d\mathbf{r} \quad (9)$$

$$C_{ij} = \sum_{k=0}^L \int_{\text{supp}(\varphi_i \varphi_j) \cap A_k} \mu_{a_k} \varphi_i \varphi_j \, d\mathbf{r} \quad (10)$$

$$M_{ij} = \frac{1}{c} \int_{\text{supp}(\varphi_i \varphi_j)} \varphi_i \varphi_j \, d\mathbf{r} \quad (11)$$

$$R_{ij} = \int_{\text{supp}(\varphi_i \varphi_j) \cap \partial\Omega} \frac{1}{2\vartheta} \varphi_i \varphi_j \, dS \quad (12)$$

where $\text{supp}(\varphi_i \varphi_j)$ expresses the part of the domain Ω where both shape functions φ_i and φ_j are non-zero, that is,

$$\text{supp}(\varphi_i \varphi_j) := \bigcup_{t \in \{N_i \in \Omega_t, N_j \in \Omega_t\}} \Omega_t. \quad (13)$$

For the collimated source model the source terms on the right-hand side of equation (8) are $F_j = \int_{\text{supp}(\varphi_j)} q_0 \varphi_j \, d\mathbf{r}$ and $G = 0$. In the case of the diffuse source model these terms are $F = 0$ and

$$G_j = \int_{\partial\Omega} \frac{-2\Gamma_s}{\vartheta} \varphi_j \, dS \quad (14)$$

where the minus sign is due to the fact that source current is inwardly directed (Schweiger *et al* 1995).

By equations (9) and (10) it is evident that matrices K and C depend on the configuration of the boundaries $\{C_\ell\}$. The problem is now to construct these matrices when the image parameters, that is, the shape coefficients γ and the values $\kappa = (\kappa_0, \dots, \kappa_L)^T$, $\mu_a = (\mu_{a_0}, \dots, \mu_{a_L})^T$ are given. Basically, this is accomplished in two main stages.

The first stage is the classification of the mesh elements Ω_m to sets of elements inside the regions A_k ($k = 0, 1, \dots, L$) and to sets of elements intercepted by the boundaries C_ℓ ($\ell = 1, 2, \dots, L$). Let

$$\mathcal{B}(C_\ell) := \{\Omega_m | \Omega_m \cap C_\ell \neq \emptyset\}$$

denote the set of elements Ω_m intercepted by the boundary C_ℓ and let

$$\mathcal{A}(A_k) := \{\Omega_m | \Omega_m \cap A_k = \Omega_m\}.$$

denote the set of elements Ω_m inside the region A_k . For the sets $\mathcal{B}(C_\ell)$ we also compute the values of the curve parameter s in the intersection points $C_\ell(s_1)$ and $C_\ell(s_2)$ for each element $\Omega_m \in \mathcal{B}(C_\ell)$ (see figure 2).

The second stage is the computation of the integrals $\int \mu_{a_k} \varphi_i \varphi_j \, d\mathbf{r}$ and $\int \kappa_k \nabla \varphi_i \cdot \nabla \varphi_j \, d\mathbf{r}$ in equations (9) and (10). Clearly, in the element set $\{\Omega_m | \Omega_m \in \text{supp}(\varphi_i \varphi_j), \Omega_m \in \mathcal{A}(A_k)\}$ the integrals over each element Ω_m are computed. The integration can be carried out by using the conventional global-to-local element mappings and Gaussian quadratures (Cuvelier and Segal 1986, Brenner and Scott 1994). Obviously, in the element set $\{\Omega_m | \Omega_m \in \mathcal{B}(C_\ell), \Omega_m \in \text{supp}(\varphi_i \varphi_j)\}$ we have to compute integrals over parts of the elements Ω_m . In this process we approximate the boundary C_ℓ with a straight line from the intersection point $C_\ell(s_1)$

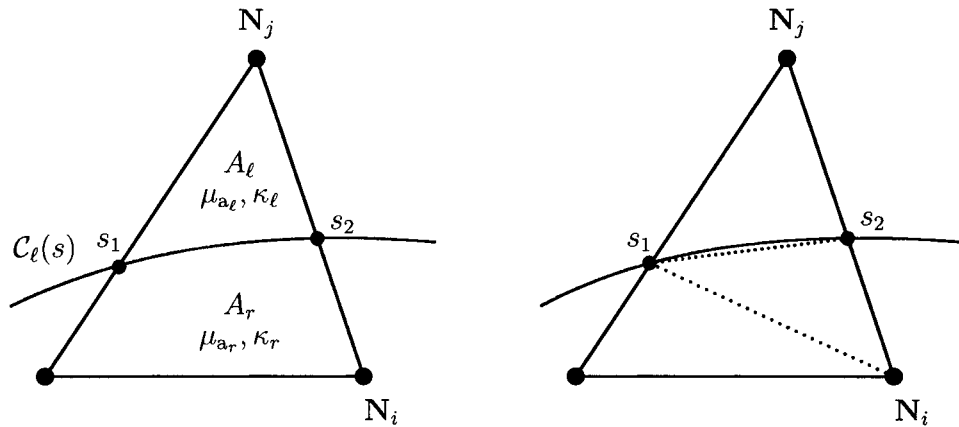


Figure 2. Left: a schematic representation of one FEM element Ω_m intercepted by the region boundary $C_\ell(s)$. The pair $(\kappa_\ell, \mu_{a_\ell})$ correspond to the values of the coefficients of equation (5) inside the region A_ℓ , and (κ_r, μ_{a_r}) are the values of the coefficients in the neighbouring region A_r respectively. $C_\ell(s_1)$ and $C_\ell(s_2)$ are the intersection points of the boundary $C_\ell(s)$ and the element edges. Right: the division of the Ω_m to three subtriangles.

to the point $C_\ell(s_2)$ and then we split the intercepted element Ω_m into three triangular parts (see figure 2). The integrals $\int \mu_{a_k} \varphi_i \varphi_j \, d\mathbf{r}$ and $\int \kappa_k \nabla \varphi_i \cdot \nabla \varphi_j \, d\mathbf{r}$ are then computed separately over the three subtriangles. This is done by mapping the functions $\varphi_i \varphi_j$ and $\nabla \varphi_i \cdot \nabla \varphi_j$ from the subtriangles to the local element and then the integrals are evaluated by using Gaussian quadratures. For more details on the subdivision of the discretization elements, see Kolehmainen *et al* (1999).

The FEM equation (8) can be solved using standard techniques such as Cholesky factorization or conjugate gradients. The relation between the solution of the FEM equation and the data can be expressed as

$$z_j = \mathcal{M}_j[\Phi_j]$$

where \mathcal{M}_j is a measurement operator and Φ_j is the solution to equation (8) for the j th source. The form of the measurement \mathcal{M}_j operator depends on the data type z_j that is used for the image reconstruction (Arridge 1999, Schweiger and Arridge 1999a). Finally, by using the notation

$$\mathbf{f} = \begin{pmatrix} \gamma \\ \kappa \\ \mu_a \end{pmatrix} \quad (15)$$

for the image parameters, we denote by

$$z = \mathcal{P}(\mathbf{f}) \quad (16)$$

the forward operator which gives the whole set of the data type $z = (z_1, \dots, \dots, z_S)^T$ for all S sources with given image parameters \mathbf{f} .

3. Inverse problem

We choose to minimize the quadratic output error functional which can be written in the discrete framework as

$$\Xi(\mathbf{f}) = \|z_{\text{meas}} - \mathcal{P}(\mathbf{f})\|_2^2 \quad (17)$$

where z_{meas} denotes the vector of the measurement data. In this paper we use the data type which consists of the real and imaginary parts of the complex measurement, that is, the data vector is of the form

$$z = (\text{Re}(\Gamma_1(\omega)), \dots, \text{Re}(\Gamma_S(\omega)), \text{Im}(\Gamma_1(\omega)), \dots, \text{Im}(\Gamma_S(\omega)))^T \quad (18)$$

where $\Gamma_j(\omega) = (\Gamma_{1,j}(\omega), \dots, \Gamma_{M,j}(\omega))$ is the vector of the complex measurements for the j th source (Jiang *et al* 1995a). In the time-resolved systems this data type is obtained by Fourier transforming the measured signals $\Gamma_{i,j}(t)$, and in the frequency-domain methods it is obtained directly from the measured phase and modulation amplitude. This type of data are most commonly used in optical tomography, although there is evidence to suggest that other types of data may be preferable, particularly in discriminating between absorption and diffusion parameters (Schweiger and Arridge 1999a). For more details on the properties of different data types which can be used for the image reconstruction in optical tomography see Schweiger and Arridge (1997, 1999a), Arridge and Schweiger (1995), Jiang *et al* (1995b) and Arridge and Lionheart (1998).

The inverse problem consists of finding the set of image parameters which minimize the cost functional (17), that is,

$$\text{find } \mathbf{f}^* \text{ such that } \Xi(\mathbf{f}^*) = \min \|\mathbf{z}_{\text{meas}} - \mathcal{P}(\mathbf{f}^*)\|_2^2. \quad (19)$$

A well-established way to solve this nonlinear optimization problem is to use Newton-type methods where we seek for \mathbf{f}^* by an iterative process. Due to the ill-posed nature of the problem (19) we use a Levenberg–Marquardt type method in which the current estimate $\mathbf{f}^{(k)}$ is updated by using an iteration

$$\mathbf{f}^{(k+1)} = \mathbf{f}^{(k)} + \mathbf{f}^{(0)} \Delta \tilde{\mathbf{f}}^{(k)} \quad (20)$$

where the update $\Delta \tilde{\mathbf{f}}^{(k)}$ is obtained as

$$\Delta \tilde{\mathbf{f}}^{(k)} = (\tilde{\mathbf{J}}^T \tilde{\mathbf{J}} + \lambda \mathbf{I})^{-1} \tilde{\mathbf{J}}^T \tilde{\mathbf{z}}. \quad (21)$$

This process is continued until we find $\mathbf{f}^{(k+1)}$ such that the stopping criteria of the iteration is fulfilled, and then we use $\mathbf{f}^* = \mathbf{f}^{(k+1)}$. The following features have been taken into account in this Levenberg–Marquardt type method:

- The real and imaginary parts of the complex measurement are of different magnitude. In order to keep the update (21) numerically stable, we have used rescaled data

$$\tilde{\mathbf{z}} = \frac{\mathbf{z}_{\text{meas}} - \mathcal{P}(\mathbf{f}^{(k)})}{\mathbf{z}_{\text{meas}}}. \quad (22)$$

- The image parameters \mathbf{f} are of different physical dimensions. In order to make the parameters dimensionless we have rescaled parameters by their initial settings, that is, the update $\Delta \tilde{\mathbf{f}}^{(k)}$ is of the form

$$\Delta \tilde{\mathbf{f}}^{(k)} = \frac{\mathbf{f}^{(k+1)} - \mathbf{f}^{(k)}}{\mathbf{f}^{(0)}}. \quad (23)$$

This normalization also improves the numerical stability of the method.

With these rescalings and with the given data type (18), the Jacobian matrix in equation (21) is of the form

$$\tilde{\mathbf{J}} = \frac{\mathbf{J}^{(k)} \text{diag}(\mathbf{f}^{(0)})}{\mathbf{z}_{\text{meas}}} \quad (24)$$

$$\mathbf{J}^{(k)} = \begin{pmatrix} \text{Re}(\mathbf{J}_\gamma^{(k)}) & \text{Re}(\mathbf{J}_\kappa^{(k)}) & \text{Re}(\mathbf{J}_{\mu_a}^{(k)}) \\ \text{Im}(\mathbf{J}_\gamma^{(k)}) & \text{Im}(\mathbf{J}_\kappa^{(k)}) & \text{Im}(\mathbf{J}_{\mu_a}^{(k)}) \end{pmatrix}. \quad (25)$$

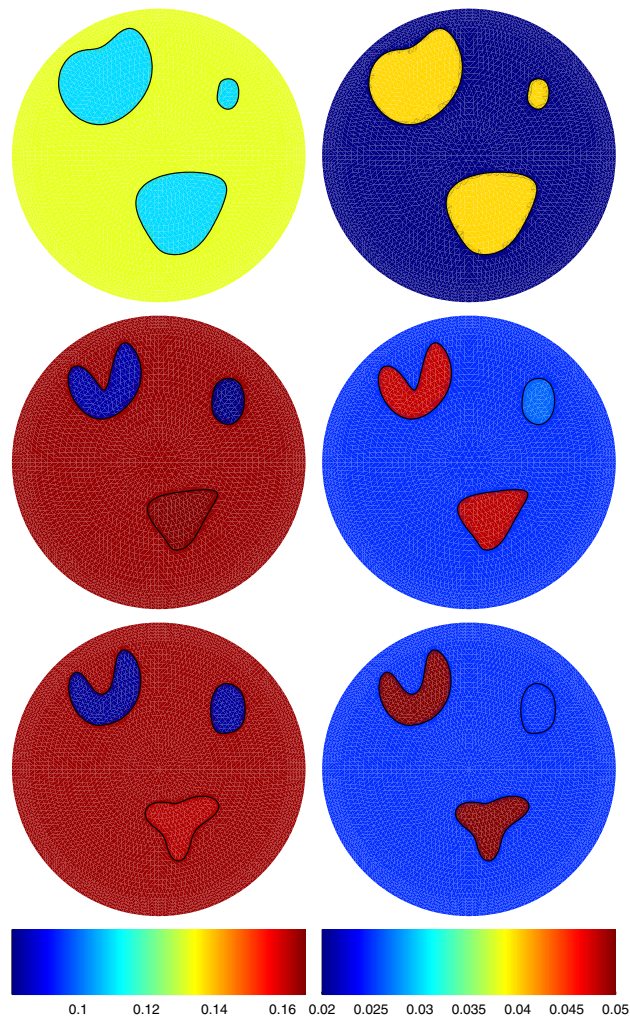


Figure 3. A test case with three boundaries $\{C_\ell\}$. Target A_1 is located up and left, A_2 is located down from the centre of Ω and A_3 is located right from the centre. The left column contains images of κ (mm) and the right column contains images of μ_a (mm⁻¹). The top row shows the initial estimates, the middle row shows the reconstructions and the bottom row the true distributions. In this case the dimension of the search space is 56. See also table 1.

The phase ϕ^s of the curve parameter s has to be fixed in equation (3) when applying equations (20) and (21) for the recovery of the image parameters \mathbf{f} . If the phase ϕ^s is not fixed we obtain a one-dimensional null space \mathcal{N}_ℓ with respect to each curve C_ℓ in the Jacobian block J_γ . This is due to the fact that the curve C_ℓ can be represented with an infinite variety of shape coefficients by adjusting the phase ϕ^s on the interval $]0, 1[$. In this paper the phase ϕ^s is fixed simply by using unequal number of sin and cos terms, i.e. we use an even number N_θ of trigonometric basis functions (Kolehmainen *et al* 1999). Details on the computation of the Jacobian (25) can be found in the appendix. In equation (21) λ is a stabilization parameter which is used for the regularization of the search direction.

Table 1. Results for the values of $\{\kappa_k, \mu_{a_k}\}$ for the test case shown in figure 3. In the heading f_i denotes either κ_k or μ_{a_k} , f_i^t denotes the true value of f_i , f_i^0 the initial guess and f_i^* the final estimate for f_i . The dimension of κ_k is [mm] and the dimension of μ_{a_k} is [mm⁻¹].

Parameter f_i	f_i^t	f_i^0	f_i^*	$\ f_i^t - f_i^0\ /\ f_i^t\ $ (%)	$\ f_i^t - f_i^*\ /\ f_i^t\ $ (%)
μ_{a_0}	0.0250	0.0200	0.0250	20.0000	0.1492
μ_{a_1}	0.0500	0.0400	0.0480	20.0000	3.9128
μ_{a_2}	0.0500	0.0400	0.0483	20.0000	3.4110
μ_{a_3}	0.0250	0.0400	0.0266	60.0000	6.5591
κ_0	0.1646	0.1323	0.1650	19.6429	0.2437
κ_1	0.0823	0.1096	0.0836	33.2237	1.6325
κ_2	0.1626	0.1096	0.1667	32.5658	2.5251
κ_3	0.0828	0.1096	0.0805	32.4013	2.8160

4. Results

In this section we consider some numerical test cases based on synthetic data of the form (18). The measurement system that the simulation is based on consists of 16 source fibres and 16 detector fibres in equiangular positions $\varepsilon_1, \zeta_1, \varepsilon_2, \zeta_2, \dots, \varepsilon_{16}, \zeta_{16}$ on the boundary $\partial\Omega$ of a circular domain Ω which has a diameter of 50 mm. In the construction of the phantom domains the values of the optical coefficients were chosen from the range of interest in medical imaging (Arridge 1999). For the absorption coefficient μ_a we used values from the range 0.025 mm⁻¹–0.05 mm⁻¹, and for the reduced scattering coefficient μ'_s we used values from the range 2 mm⁻¹–4 mm⁻¹. The values for the diffusion coefficient were computed by using the relation $\kappa = [3(\mu_a + \mu'_s)]^{-1}$. The subdomains were bounded by trigonometric boundaries. In the FEM computations we used piecewise linear basis functions φ_i . In the generation of the synthetic data we discretized the object domain Ω to $P = 8600$ triangular elements Ω_p with total number of $D = 4429$ vertex nodes. The simulated data were computed by using a single frequency $\omega = 300$ MHz, and a multiplicative random noise with standard deviation of 1% of the measured signal was added to the simulated data (Arridge *et al* 1995).

In the image reconstruction process we used a mesh which consisted of $P = 6776$ triangular elements Ω_p with a total of $D = 3517$ vertex nodes. In the following test reconstructions we used $N_\theta = 8$ basis functions of the form (3) for the representation of the region boundaries. In each simulation the stabilization parameter λ was chosen based on convergence. The iterations were carried out until full convergence was obtained, which was verified by monitoring the error norm $\|\tilde{z}\|$ and the behaviour of the image parameters. The results for the three different test cases are shown in figures 3, 5 and 6. In each of these figures the images in the bottom row are the true distributions of κ (left) and μ_a (right), the middle row shows the reconstructions f^* , and the top row shows the initial estimates $f^{(0)}$. We also show the convergence properties of the method, that is the behaviour of the error norms and parameter values with respect to the iteration index for the first test case.

The results of the first test case are shown in figure 3. The region A_1 , which is located up and left, has significant contrast in both the diffusion and absorption coefficients with respect to the surrounding region A_0 (see table 1). The region A_2 , which is located on the lower part of Ω , has significant contrast in the absorption coefficient and only a weak contrast in the diffusion coefficient with respect to the surrounding region A_0 . The region A_3 , which is located up and right from the centre of Ω , has significant contrast in the diffusion coefficient

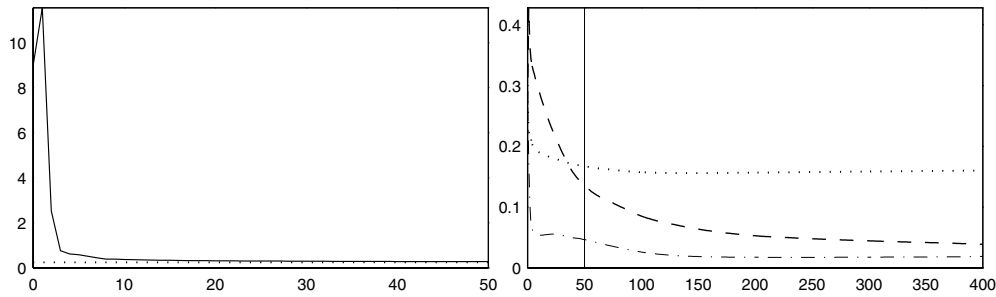


Figure 4. Convergence behaviour for the test case in figure 3. Left: $\|\tilde{z}\|$ versus iteration index k for the first 50 iterations. The dotted curve shows the final value $\|\tilde{z}\| = 0.25$. Right: $\|\kappa^{(k)} - \kappa^{(\text{true})}\|/\|\kappa^{(\text{true})}\|$ versus iteration index k is shown with the dash-dot curve, $\|\mu_{\mathbf{a}}^{(k)} - \mu_{\mathbf{a}}^{(\text{true})}\|/\|\mu_{\mathbf{a}}^{(\text{true})}\|$ with the dashed curve and $\|\gamma^{(k)} - \gamma^+\|/\|\gamma^{(\text{true})}\|$ with the dotted curve, where γ^+ denotes the shape coefficients corresponding to the basis functions $\theta_n(s)$, $n = 1, \dots, 8$ for the true boundaries $\{\mathcal{C}_\ell\}$.

but no contrast in the absorption coefficient. The initial values of the diffusion and absorption coefficients were chosen sufficiently far from the true values leading to initial estimation error norms approximately in the range 20–60% (see table 1).

As can be seen from figure 3, the shapes of the boundaries of the regions A_1 – A_3 are found with almost equally good accuracy despite the differences in the contrast of the regions. The diffusion and absorption coefficients $\{\kappa_k, \mu_{a_k}\}$ are also found with good accuracy resulting in final estimation error norms in the range 0–7% (see table 1). In this simulation the value of the stabilization parameter was $\lambda = 1$ and the number of iterations was 400. The behaviour of the error norm $\|\tilde{z}\|$ versus iteration index k is shown on the left-hand side of figure 4 for 50 iterations from the beginning of the process. As can be seen, in the beginning the iteration converges rapidly close to the minimum value of the objective function and after that the convergence of the iteration is very slow. The initial error norm was $\|\tilde{z}\| = 8.99$ and the final value was $\|\tilde{z}\| = 0.25$. The image on the right-hand side of figure 4 shows the behaviour of the error norms $\|\kappa^{(k)} - \kappa^{(\text{true})}\|/\|\kappa^{(\text{true})}\|$ (dash-dot curve), $\|\mu_{\mathbf{a}}^{(k)} - \mu_{\mathbf{a}}^{(\text{true})}\|/\|\mu_{\mathbf{a}}^{(\text{true})}\|$ (dashed curve) and $\|\gamma^{(k)} - \gamma^+\|/\|\gamma^{(\text{true})}\|$ (dotted curve) with respect to the iteration index k , where γ^+ denotes the shape coefficients corresponding to the orthonormal basis functions $\{\theta_n, n = 1, \dots, 8\}$ for the true boundaries $\{\mathcal{C}_\ell\}$. Note that γ^+ and $\gamma^{(\text{true})}$ have different dimensions. As can be seen, the shape coefficients γ converge close to their final values in approximately 100 iterations. The change in the boundary configuration is very small after this point. This observation was verified by inspecting the configuration of the boundaries after each iteration. The values of the coefficients κ and $\mu_{\mathbf{a}}$ have very slow convergence. It is worth noting that they still exhibit significant changes on the part of the iteration where $\|\tilde{z}\|$ decreases very slowly. These results suggest that the objective functional $\Xi(f)$ exhibits an almost flat elongated plateau, which is oriented especially in the directions specified by κ and $\mu_{\mathbf{a}}$, around the minimum.

The second test case, which has some resemblance to the cross section of an infant's head, is shown in figure 5 and table 2. The initial configuration of the four nested regions A_0 – A_3 , which are in respective order from $\partial\Omega$ towards the centre of Ω , is shown in the top row in figure 5. In the initial estimate we assumed that the correct values of κ_0 and μ_{a_0} in the background region A_0 were known *a priori* and for other regions the values of the diffusion and absorption were chosen relatively close to the true values, resulting in initial errors in the range 10–20%.

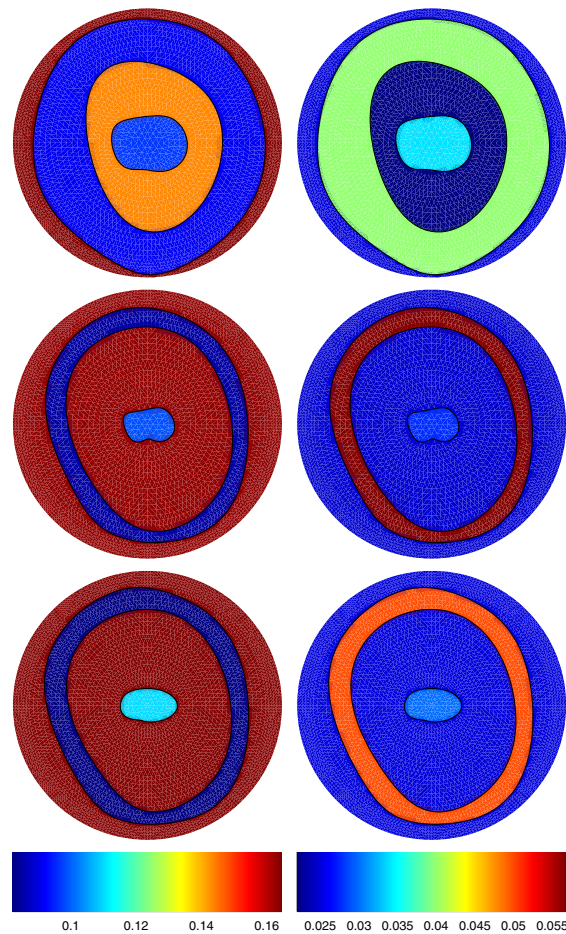


Figure 5. A test case with three nested boundaries. The regions A_0 – A_3 are in respective order from $\partial\Omega$ towards the centre of Ω . The left column shows images of κ (mm) and the right column shows images of μ_a (mm^{-1}). Top row shows the initial estimates, the middle row shows the reconstructions and the bottom row the true distributions. In this nested regions case the dimension of the search space is 56. See also table 2.

The resulting reconstruction is shown in the middle row of figure 5. The stabilization parameter was $\lambda = 120$ and the number of iterations was 650. As can be seen, the ‘skin–skull’ boundary \mathcal{C}_1 and the ‘skull–brain’ boundary \mathcal{C}_2 are found with good accuracy, whereas the innermost boundary \mathcal{C}_3 is found less accurately. This was to be expected since the sensitivity of the measured data is low with respect to coefficients near the centre of Ω due to the highly scattering and absorbing ‘skull’ region A_1 . In this simulation the recovery of the values of the diffusion and absorption coefficients $\{\kappa_k, \mu_{a_k}\}$ is not as good as in the previous case. In this simulation the initial error norm was $\|\tilde{z}\| = 17.95$ and the final value was $\|\tilde{z}\| = 0.44$.

The proposed method relies on the assumption that we have some initial estimate for the configuration of the domain Ω . In figures 3–5 we assumed that the number and approximate locations of the regions $\{A_k\}$ were known in the initial estimates and we obtained relatively good reconstructions.

Table 2. Results for the values of $\{\kappa_k, \mu_{a_k}\}$ for the nested regions case shown in figure 5. In the heading f_i denotes either κ_k or μ_{a_k} , f_i^t denotes the true value of f_i , f_i^0 the initial guess and f_i^* the final estimate for f_i . The dimension of κ_k is [mm] and the dimension of μ_{a_k} is [mm^{-1}].

Parameter f_i	f_i^t	f_i^0	f_i^*	$\ f_i^t - f_i^0\ /\ f_i^t\ $ (%)	$\ f_i^t - f_i^*\ /\ f_i^t\ $ (%)
μ_{a_0}	0.0250	0.0250	0.0247	0	1.3572
μ_{a_1}	0.0500	0.0400	0.0568	20.0000	13.5980
μ_{a_2}	0.0250	0.0220	0.0247	12.0000	1.2662
μ_{a_3}	0.0300	0.0340	0.0277	13.3333	7.6067
κ_0	0.1646	0.1646	0.1635	0	0.6585
κ_1	0.0823	0.0916	0.0850	11.2637	3.3330
κ_2	0.1646	0.1436	0.1632	12.7907	0.8554
κ_3	0.1100	0.0971	0.0990	11.7647	10.0390

Table 3. Results for the values of diffusion and absorption coefficients for the background region A_0 and for the region A_1 , which is located on the right-hand side of Ω in figure 6. In the heading f_i denotes either κ_k or μ_{a_k} , f_i^t denotes the true value of f_i , f_i^0 the initial guess and f_i^* the final estimate for f_i . The dimension of κ_k is [mm] and the dimension of μ_{a_k} is [mm^{-1}].

Parameter f_i	f_i^t	f_i^0	f_i^*	$\ f_i^t - f_i^0\ /\ f_i^t\ $ (%)	$\ f_i^t - f_i^*\ /\ f_i^t\ $ (%)
μ_{a_0}	0.0250	0.0200	0.0250	20.0000	0.0913
μ_{a_1}	0.0500	0.0400	0.0478	20.0000	4.3182
κ_0	0.1646	0.1468	0.1646	10.7930	0.0045
κ_1	0.0823	0.0942	0.0865	14.4068	5.1186

The results for the third test case are shown in figure 6. In this case the true configuration consists of regions A_0 – A_3 where A_1 is the bean-shaped region on the right-hand side of Ω , region A_2 is the larger bean-shaped object in the left-hand side of Ω and A_3 is the smaller anomaly within the region A_2 . Regions A_1 and A_2 have contrast in both coefficients with respect to the background A_0 , and region A_3 has contrast in both coefficients with respect to the region A_2 . In the initial estimate we assumed that only one region exists, namely the region $A_{2,3}$ on the left-hand side of Ω (see the top row in figure 6). Basically, this situation can be viewed as a simple example of a case in which a region does not have constant values of diffusion and absorption.

From the reconstructed images it can be seen that the boundary of the region A_1 is found with relatively good accuracy, and in addition, the reconstructed values of the diffusion and absorption in regions A_0 and A_1 are close to the correct values (see table 3). The reconstructed boundary of the region $A_{2,3}$ is relatively close to the true boundary of the region A_2 , and the reconstructed values of $\kappa_{2,3} = 0.1020$ mm and $\mu_{a_{2,3}} = 0.0429$ mm^{-1} fall approximately midway between the true values $(\kappa_2, \kappa_3) = (0.1098, 0.0823)$ mm and $(\mu_{a_2}, \mu_{a_3}) = (0.0350, 0.0500)$ mm^{-1} . This result indicates that the method would also lead to useful reconstructions in cases in which the largest contrast in diffusion and absorption exist over the boundaries $\{C_\ell\}$ of regions $\{A_k\}$ which may be spatially varying in diffusion and absorption coefficients. In this simulation the stabilization parameter was $\lambda = 5$ and the number of iterations was 400. The initial error norm was $\|\tilde{z}\| = 11.72$ and the final value of the error norm was $\|\tilde{z}\| = 0.36$. We also conducted several test cases in which we made large errors in the locations of the targets in the initial estimates. In these cases the method exhibited stability problems and gave poor reconstructions. Similar types of problems of poor initial estimates also occurred in the recovery of the region boundaries in the work of Kolehmainen *et al* (1999).

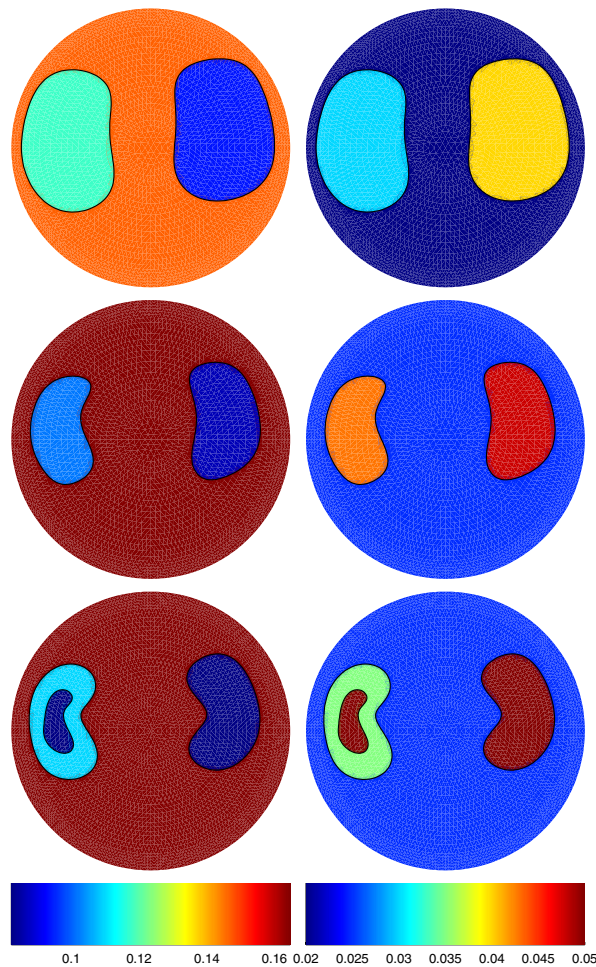


Figure 6. Bottom row: a test case with regions A_0 – A_3 . Region A_1 is located on the right-hand side of Ω , A_2 is located on the left-hand side of Ω and A_3 is located inside A_2 . The left column contains images of κ (1/mm) and the right column contains images of μ_a (1/mm⁻¹). Top row: in the initial estimate we have assumed that there exists only a single region $A_{2,3}$ on the left-hand side of Ω . Middle row: reconstructed images of κ and μ_a . In this case the dimension of the search space is 38. See also table 3.

5. Conclusions

Based on the work in Kolehmainen *et al* (1999), we have proposed a new reconstruction method for the inverse problem in optical diffusion tomography. The goal in the proposed method is to reconstruct simultaneously the shapes and locations of the smooth boundaries of the piecewise-constant tissue regions and the values of the diffusion and absorption coefficients within these regions. This inverse problem was approached as an optimization problem in which the configuration of image parameters which minimize the error norm between measured and predicted data was solved by using an iterative Levenberg–Marquardt type method. The performance of the method was evaluated by using noisy synthetic frequency-domain data.

Based on the simulations it seems that the method results in relatively good recovery of the diffusion and absorption distributions in cases in which we have approximate *a priori* knowledge about the locations of the distinct tissue regions. It also seems that the method gives useful reconstructions in a case in which the diffusion and absorption may have small spatial variations within the tissue regions. We suggest that the method could be used, for example, for the construction of a simple approximate model of the object in a two-step reconstruction scheme (Schweiger and Arridge 1999b). In the first step, an approximate configuration of different organs and global averages of the parameters within these organs could be reconstructed by using the proposed method, and in the second step smaller anomalies could be reconstructed by carrying out a conventional local-basis function reconstruction which uses the first-stage reconstruction as an initial estimate. Such a method would be useful, for example, in the imaging of the infant head in the absence of exact anatomical data. It is also worth noting that the proposed method can be easily modified to an anatomically constrained reconstruction method in a case in which the exact configuration of the region boundaries is available, for example from an MRI scan of the object.

A weak point of the method is that it has very slow convergence. The Levenberg–Marquardt type method, in which the constant stabilization parameter was chosen to be large enough to secure convergence, converged in a few iterations close to the minimum value of the objective function, and after that the convergence was extremely slow. It is therefore worth investigating to what extent the convergence can be improved by using more efficient optimization methods. The strategies which may be considered include adaptive methods in which the stabilization parameter is different for each parameter; in addition, these parameters are made adaptive so that they vanish gradually (Kelley 1999). However, these methods necessitate a more thorough analysis of the geometry of the objective functional. Another weak point of the method is that it gives poor reconstructions when there are large errors in the locations of the tissue regions in the initial estimate. In some of the worst cases the method exhibited a tendency to give unfeasible solutions due to the fact that the given boundary representation does not exclude self-intersecting boundaries. Depending on the topological requirements, these problems could be partially avoided in some cases by using some other differentiable expansion for the boundary curves. Also, in these cases of poor initial estimate it would be possible to look for an approximate configuration of the initial region by carrying out a normal local-basis function reconstruction as a first step.

The results presented in this paper utilize data from a 2D model to reconstruct 2D images. Whereas this is sufficient to demonstrate the method, it is well known that optical tomography must be considered a 3D problem (Schweiger and Arridge 1998). In principle the method presented here can be extended to 3D. The validity of a 3D FEM model for optical tomography has been shown in simulations in Schweiger and Arridge (1998) and using measured data in Arridge *et al* (2000). In order to utilize the shape recovery we need to derive a shape representation for surfaces, and characterize the inverse problem as the recovery of parameters of these surfaces. A natural choice is spherical harmonics, such as have been successfully used for the representation of anatomical structures in other areas of medical imaging (Brechtbühler *et al* 1995, Kelemen 1995). Work on this scheme is under way. The intersection of boundaries of parametrically defined surfaces with FEM volume elements such as tetrahedra will follow the general methods described here, although the technical issues will be somewhat more complex. We expect to report on this extension in a subsequent publication.

In the test cases of this paper we used a relatively small number of basis functions for the curve representation in the inverse problem. If one wishes to use more basis functions, the ill-posedness of the inverse problem will increase rapidly and at some point the method will necessitate regularization. One possibility would be to use subspace regularization type

methods (Vauhkonen *et al* 1997, 1998) which are based on probabilistic approximations of the parameter distributions. Another aspect that is worth further investigation is the dependence of the performance of the method on the different data types which can be used for the image reconstruction in optical tomography.

Acknowledgments

This work was supported by the Saastamoinen Foundation, the Jenny and Antti Wihuri Foundation and the Savo Foundation for Advanced Technology. S Arridge acknowledges the support of the Wellcome Trust.

Appendix. Computation of the Jacobian matrix

Let us consider the computation of the augmented Jacobian in a columnwise manner. Let f_i denote the i th component of the image parameter vector f . By using the notation

$$T(f) := K(\kappa, \gamma) + C(\mu_a, \gamma)$$

in equation (8) and then differentiating it with respect to the parameter f_i , we obtain

$$T \frac{\partial \Phi}{\partial f_i} = -\frac{\partial T}{\partial f_i} \Phi. \quad (\text{A.1})$$

By solving equation (A.1) for the j th light source we obtain

$$\frac{\partial \Phi_j}{\partial f_i} = -T^{-1} \frac{\partial T}{\partial f_i} \Phi_j. \quad (\text{A.2})$$

By applying the discrete boundary operator \mathcal{M}_j to equation (A.2), we obtain the vector

$$\rho_{j,m} = \mathcal{M}_j \left[\frac{\partial \Phi_j}{\partial f_i} \right] \quad (\text{A.3})$$

which is the j th block of the m th column of the augmented Jacobian (25). In equation (A.3) we have assumed that the boundary operator \mathcal{M} is independent of the image parameter f_i .

In equations (A.1)–(A.3) f_i is either $\gamma_n^{x_\ell}$, $\gamma_n^{y_\ell}$, κ_k or μ_{a_k} . The elements of the derivatives of the matrix T with respect to the boundary shape coefficients are obtained as

$$\begin{aligned} \left(\frac{\partial T}{\partial \gamma_n^{x_\ell}} \right)_{ij} = & \sum_{m | \Omega_m \in B(\mathcal{C}_\ell) \cap \text{supp}(\varphi_i \varphi_j)} \left((\mu_{a_\ell} - \mu_{a_r}) \int_{s_1}^{s_2} \varphi_i \varphi_j \dot{y}_\ell(s) \theta_n^x(s) \, ds \right. \\ & \left. + (\kappa_\ell - \kappa_r) \int_{s_1}^{s_2} \nabla \varphi_i \cdot \nabla \varphi_j \dot{y}_\ell(s) \theta_n^x(s) \, ds \right) \end{aligned} \quad (\text{A.4})$$

and

$$\begin{aligned} \left(\frac{\partial T}{\partial \gamma_n^{y_\ell}} \right)_{ij} = & \sum_{m | \Omega_m \in B(\mathcal{C}_\ell) \cap \text{supp}(\varphi_i \varphi_j)} \left(-(\mu_{a_\ell} - \mu_{a_r}) \int_{s_1}^{s_2} \varphi_i \varphi_j \dot{x}_\ell(s) \theta_n^y(s) \, ds \right. \\ & \left. - (\kappa_\ell - \kappa_r) \int_{s_1}^{s_2} \nabla \varphi_i \cdot \nabla \varphi_j \dot{x}_\ell(s) \theta_n^y(s) \, ds \right). \end{aligned} \quad (\text{A.5})$$

In equations (A.4) and (A.5) the values $(\kappa_\ell, \mu_{a_\ell})$ are the coefficients in the region A_ℓ which is closed by the curve \mathcal{C}_ℓ and the (κ_r, μ_{a_r}) are the values in the surrounding region A_r (see figure 2). The limits of integration s_1 and s_2 are the values of the curve parameter in the intersection points of the element edges and boundary curve \mathcal{C}_ℓ in each of the elements Ω_m . The derivation of equations (A.4) and (A.5) can be found in Kolehmainen *et al* (1999).

By inspecting equations (9) and (10), it can be seen that the elements of the matrices $\frac{\partial T}{\partial \kappa_k}$ and $\frac{\partial T}{\partial \mu_{ak}}$ are obtained as

$$\left(\frac{\partial T}{\partial \kappa_k}\right)_{ij} = \int_{\text{supp}(\varphi_i \varphi_j) \cap A_k} \nabla \varphi_i \cdot \nabla \varphi_j \, d\mathbf{r}$$

$$\left(\frac{\partial T}{\partial \mu_{ak}}\right)_{ij} = \int_{\text{supp}(\varphi_i \varphi_j) \cap A_k} \varphi_i \varphi_j \, d\mathbf{r}.$$

References

- Ackroyd R T 1997 *Finite Element Methods for Particle Transport: Applications to Reactor and Radiation Physics* (Taunton: Research Studies Press)
- Aronson R 1995 Boundary conditions for diffusion of light *J. Opt. Soc. Am. A* **12** 2532–9
- Arridge S R 1999 Optical tomography in medical imaging *Inverse Problems* **15** R41–R93
- Arridge S R, Hebden J C, Schweiger M, Schmidt F E W, Fry M E, Hillman E M C, Dehghani H and Delpy D T 2000 A method for three-dimensional time-resolved optical tomography *Int. J. Imaging Sci. Technol.* **11** 2–11
- Arridge S R, Hiraoka M and Schweiger M 1995 Statistical basis for the determination of optical pathlength in tissue *Phys. Med. Biol.* **40** 1539–58
- Arridge S R and Lionheart W R B 1998 Non-uniqueness in diffusion-based optical tomography *Opt. Lett.* **23** 882–4
- Arridge S R and Schweiger M 1995 Direct calculation of the moments of the distribution of photon time of flight in tissue with a finite-element method *Appl. Opt.* **34** 2683–7
- 1999 A general framework for iterative reconstruction algorithms in optical tomography, using a finite element method *Computational Radiology and Imaging: Therapy and Diagnosis (IMA Volumes in Mathematics and its Applications 110)* ed C Borgers and F Natterer (Berlin: Springer) pp 45–70
- Brechbühler Ch, Gerig G and Kübler O 1995 Parametrization of closed surfaces for 3-D shape description *Computer Vision Image Understanding* **61** 154–70
- Brenner S C and Scott L R 1994 *The Mathematical Theory of Finite Element Methods* (Berlin: Springer)
- Case M C and Zweifel P F 1967 *Linear Transport Theory* (New York: Addison-Wesley)
- Chandrasekhar S 1950 *Radiative Transfer* (London: Oxford University Press)
- Cuvelier C and Segal A 1986 *Finite Element Methods and Navier–Stokes Equations* (Dordrecht: Reidel)
- Davison B 1957 *Neutron Transport Theory* (London: Oxford University Press)
- Dorn O 1998 A transport-backtransport method for optical tomography *Inverse Problems* **14** 1107–30
- Duderstadt J J and Martin W R 1979 *Transport Theory* (New York: Wiley)
- Fantini S, Franceschini M A, Gaida G, Gratton E, Jess H, Mantulin W W, Moesta K T, Schlag P M and Kaschke M 1996 Frequency-domain optical mammography: edge effect corrections *Med. Phys.* **23** 149–57
- Gryazyn Y A, Klibanov M V and Lucas T R 1999 Imaging the diffusion coefficient in a parabolic inverse problem in optical tomography *Inverse Problems* **15** 373–97
- Hebden J C, Arridge S R and Delpy D T 1997 Optical imaging in medicine: I. Experimental techniques *Phys. Med. Biol.* **42** 825–40
- Hielscher A H, Klose A D and Hanson K M 1999 Gradient-based iterative image reconstruction scheme for time-resolved optical tomography *IEEE Trans. Med. Imaging* **18** 262–71
- Ishimaru A 1978 *Wave Propagation and Scattering in Random Media* vol 1 (New York: Academic)
- Jess H, Erdl H, Moesta K T, Fantini S, Franceschini M A and Gratton E 1996 Intensity modulated breast imaging: technology and clinical pilot study results *OSA TOPS on Advances in Optical Imaging and Photon Migration* vol 2 ed R R Alfano and J G Fujimoto (Washington, DC: Optical Society of America) pp 126–9
- Jiang H, Paulsen K D, Osterberg U L, Pogue B W and Patterson M S 1995 Optical image reconstruction using frequency-domain data: simulations and experiments *J. Opt. Soc. Am. A* **13** 253–66
- 1995 Simultaneous reconstruction of absorption and scattering profiles in turbid media from near-infrared frequency-domain data *Opt. Lett.* **20** 2128–30
- Kelemen A, Szekely G and Gerig G 1995 Three-dimensional model-based segmentation *IEEE Trans. Med. Imaging* **18** 828–39
- Kelley C T 1999 *Iterative Methods for Optimization* (Philadelphia: SIAM)
- Kolehmainen V, Arridge S R, Lionheart W R B, Vauhkonen M and Kaipio J P 1999 Recovery of region boundaries of piecewise constant coefficients of an elliptic PDE from boundary data *Inverse Problems* **15** 1375–91
- Moesta K T, Fantini S, Jess H, Totkas S, Franceschini M A, Kaschke M and Schlag P M 1998 Contrast features of breast cancer in frequency-domain laser scanning mammography *J. Biomed. Opt.* **3** 129–36

- Schweiger M and Arridge S R 1997 Optimal data types in optical tomography *Information Processing in Medical Imaging (IPMI'97 Proc.) (Lecture Notes in Computer Science 1230)* (Berlin: Springer) pp 71–84
- Schweiger M and Arridge S R 1998 Comparison of 2D and 3D reconstruction algorithms in optical tomography *Appl. Opt.* **37** 7419–28
- 1999a Application of temporal filters to time resolved data in optical tomography *Phys. Med. Biol.* **44** 1699–717
- 1999b Optical tomographic reconstruction in a complex head model using a priori region boundary information *Phys. Med. Biol.* **44** 2703–21
- Schweiger M, Arridge S R, Hiraoka M and Delpy D T 1995 The finite element model for the propagation of light in scattering media: boundary and source conditions *Med. Phys.* **22** 1779–2
- van Houten J P, Benaron D A, Splilman S and Stevenson D K 1996 Imaging brain injury using time-resolved near-infrared light scanning *Pediatr. Res.* **39** 470–6
- Vauhkonen M, Kaipio J P, Somersalo E and Karjalainen P A 1996 Electrical impedance tomography with basis constraints *Inverse Problems* **13** 523–30
- Vauhkonen M, Vadász D, Karjalainen P A, Somersalo E and Kaipio J P 1998 Tikhonov regularization and prior information in electrical impedance tomography *IEEE Trans. Med. Imaging* **17** 285–93
- Weinberg A M and Wigner E P 1958 *The Physical Theory of Neutron Chain Reactors* (Chicago: University of Chicago Press)
- Wyatt J S, Cope M, Delpy D T, Richardson C E, Edwards A D, Wray S C and Reynolds E O R 1990 Quantitation of cerebral blood volume in newborn infants by near infrared spectroscopy *J. Appl. Physiol.* **68** 1086–91